Materials
Horizons

COMMUNICATION

Cite this: DOI: 10.1039/d5mh00731c

Received 23rd April 2025,
Accepted 26th June 2025

DOI: 10.1039/d5mh00731c

rsc.li/materials-horizons

An intelligent tactile imaging-recognition sensor system enabled *via* a methoxynitrobenzene-salicylaldehyde fluorescent material†

Zihan Liu, Xinyi Zhao, Yuai Duan, Yaping Li, Zhijia Wang, Zixuan Wang, Jiarong Zhang, Jing Yuan, Hua Geng and Tianyu Han*

Tactile sensors utilizing functional materials decode surface textures for object recognition. Herein, we engineer a donor–acceptor fluorescent material, MNIMP, that synergizes aggregation-induced emission (AIE) and twisted intramolecular charge transfer (TICT) mechanisms. Contact-induced nanoflake assembly on the MNIMP film triggers fluorescence amplification mediated by the combined AIE and TICT effects, through which the surface morphology of textured objects can be accurately visualized as fluorescent patterns. MNIMP maps micro-textures of materials such as rubber, fabrics, and elastic polymers under tactile pressure with kPa-level sensitivity, seamlessly integrating visual and tactile perceptions. These fluorescent signatures can be recognized using a deep-learning model with >98% accuracy. Hardware integration with the embedded algorithm model creates an intelligent tactile sensor system performing concurrent contact imaging, data analysis, and classification. This intelligent platform demonstrates micron-scale resolution and cost-effective manufacturability while maintaining high signal fidelity across diverse target objects.

New concepts

This work presents an intelligent tactile sensor system enabled *via* a fluorescent material **MNIMP**. By integrating aggregation-induced emission (AIE) with twisted intramolecular charge transfer (TICT) mechanisms, the material demonstrates enhanced sensitivity and resolution through pronounced fluorescence responses to self-assembly structures. The sensor effectively combines visual and tactile perceptions by visualizing the surface texture details under minimal contact force, requiring only facile fabrication processes and basic imaging equipment. This approach significantly reduces signal complexity and computational requirements typically associated with multi-dimensional signal processing intrinsic to multimodal tactile sensors, while maintaining high classification accuracy across diverse textured targets. Furthermore, this work establishes an intelligent tactile sensor system integrating **MNIMP** with hardware components, enabling real-time fluorescence imaging and target recognition through deep learning-based image analysis. The immediate visual feedback and compatibility with artificial intelligence frameworks of the material suggest promising applications in human–machine interaction, robotic manipulation, and integrated visual–haptic systems, advancing the development of intelligent sensory technologies.

Introduction

The generation of human tactile sense is a complex physiological process involving synergistic effects between skin, touch receptors, the nervous system, and the brain.[1–3] Upon physical contact between skin and objects, the brain receives signals and translates them into multiple sensations such as ‘‘hard’’, ‘‘soft’’, ‘‘hot’’, ‘‘cold’’, and surface features.[4] In most cases, the human skin's perception of surface texture remains imprecise, providing only a preliminary judgment of roughness. When materials are similar in composition and surface textures have subtle details, accurate identification through the skin becomes difficult.[5,6] Moreover, tactile perception of textural features is particularly challenging for people with certain diseases or arm disabilities.[7,8] Furthermore, physical contact-based texture sensing is inappropriate in complex or dangerous scenarios. Therefore, designing texture recognition technologies is critically important. In recent years, these technologies have focused on enabling information exchange between intelligent devices and the external environment, demonstrating potential in human–robot interaction,[9,10] dynamic target detection,[11,12] and unmanned aerial vehicles.[13] However, most studies rely on machine vision or computer-based imaging techniques, where texture images are susceptible to environmental factors and camera conditions, compromising reliability and robustness.[14]

Perceiving texture information through tactile sensors represents an alternative approach, with their hardware core

---

Department of Chemistry, Capital Normal University, Beijing, 100048, China. E-mail: hanty@cnu.edu.cn

† Electronic supplementary information (ESI) available. CCDC 2457590. For ESI and crystallographic data in CIF or other electronic format see DOI: https://doi.org/10.1039/d5mh00731c

consisting of tailor-made tactile sensing materials or photoelectric devices.[15,16] These sensors primarily operate on established principles including capacitance,[17,18] piezoresistivity,[19,20] piezoelectricity,[21,22] and inductance.[23,24] Their operation typically requires batteries and circuits, hindering energy/cost efficiency while limiting flexibility and portability. Developing wireless battery-free sensors with lightweight designs and flexible/stretchable substrates is therefore an ideal solution for wearable and user-friendly applications.[25–28] Triboelectric tactile sensors based on contact electrification are considered a typical energy-efficient option.[29] They detect surface textures *via* electrostatic induction and achieve high recognition accuracy through machine-learning-based data processing.[30–32] However, such sensors require repeated friction prior to perception, risking damage to fragile materials or hyperfine surface structures. Additionally, most generate multi-channel output signals that are non-intuitive and complex, complicating subsequent data processing.[33,34]

Literature reports suggest that integrating multimodal sensory inputs (*e.g.*, combining visual and tactile perception mechanisms) represents a viable approach to enhancing both sensitivity and perceptual comprehensiveness in tactile sensors.[35,36] However, this strategy introduces three primary challenges: (i) an exponential increase in data complexity and computational demands arising from multidimensional signal processing, (ii) compromised real-time feedback capability due to parallel data stream synchronization requirements, and (iii) amplified interference susceptibility in predictive decision-making algorithms. Furthermore, most high-performance tactile sensors currently rely on sophisticated fabrication processes involving micro/nano-patterning techniques and advanced materials engineering, resulting in prohibitively high production costs.[37,38] These combined technical and economic barriers significantly hinder commercial scalability and mass manufacturing feasibility.

The utilization of optical signals represents a feasible solution, as it simplifies signal conversion while eliminating the need for wires and power sources.[39] Such devices are therefore easily miniaturized, facilitating integration into peripheral intelligent hardware for practical applications.[40–42] Over the past decades, scientists have explored pressure sensors based on mechanochromic compounds.[43–46] These compounds exhibit emission/color changes in response to mechanical forces (*e.g.*, pressing, grinding, or stretching) due to mechanical-stress-induced changes in their packing or chemical structures.[47,48] However, they generally lack sensitivity and require high pressure up to the GPa level, making them unsuitable for tactile sensing with lower contact pressures.[49,50] Recently, highly sensitive mechanochromic pressure sensors have emerged, enabling tactile sensing and fingertip pressure detection.[51,52] Their molecular design typically employs donor–acceptor (D–A) or donor–π–acceptor (D–π–A) frameworks, which promote twisted intramolecular charge transfer (TICT) emission and self-assembly behavior.[53–56] The TICT state is characterized by emission sensitivity to local polarity and electron-donating/withdrawing effects, which alter the S_1/S_0 energy gap and induce significant emission changes.[57–60] Additionally, molecular design inherent in aggregation-induced emission (AIE) offers a pathway to fabricate pressure-sensitive materials with high sensitivity.[61,62] On the one hand, their highly twisted molecular conformations can be flattened under pressure, inducing π–π stacking and resulting in a bathochromic shift or emission quenching.[59] On the other hand, mechanical stimulation rearranges aggregated molecules, altering the AIE efficiency.[63,64] Both mechanisms involve conformational changes to which TICT fluorescence is highly sensitive.[57,65] Specifically, twisted conformations enhance TICT with bathochromic shifts and reduced intensity, whereas flattened conformations reverse this trend.[57]

Combining literature reports with our previous work, the fusion of AIE and TICT can greatly improve pressure sensitivity, as synthesized materials may exhibit notable responses to slight changes in torsion angle (molecular conformation) or self-assembly structure.[66–68] The detection limit for mechanical stimulation can reach 0.1 N or MPa levels, within the range of typical contact forces.[69,70] Thus, developing tactile sensors *via* this strategy is feasible.

Herein, we design and synthesize a D–A-type methoxynitrobenzene-salicylaldehyde Schiff base (**MNIMP**) with AIE and TICT characteristics. **MNIMP** self-assembles into nanostructures upon physical contact with various target objects, resulting in emission enhancement. Due to surface roughness, the contact degree between the **MNIMP** film and target objects varies significantly, generating fluorescent patterns that replicate the objects' surface textures. Using machine-learning algorithms, the **MNIMP** film can identify different target objects non-destructively, serving as an efficient tactile sensor with kPa level sensitivity. A smart system is built based on intelligent hardware, which combines texture imaging, image-processing, and machine-learning-based recognition into one platform, enabling high accuracy in object identification. The proposed sensing platform demonstrates threefold advantages through its streamlined design: first, the simplified manufacturing protocol enables cost-effective film production using drop-casting method. Second, the system achieves fast response times through instantaneous fluorescence imaging, ensuring both high resolution and real-time target detection. Third, the synchronized integration of embedded deep-learning algorithms (convolutional neural networks with adaptive pooling layers) provides enhanced signal processing capabilities.

Experimental details

Synthesis and structural analysis

The synthetic route of **MNIMP** is indicated as follows. To a 500 mL round-bottom flask containing salicylaldehyde (30 mmol, 3.6 g) and 2-methoxy-4-nitroaniline (30 mmol, 5.00 g) was added 200 mL anhydrous ethanol, followed by dropwise addition of 60 μL acetic acid. The mixture was stirred until the reactants were fully dissolved, and then heated to 60 °C. Following 8 hours of reaction, the mixture was cooled to room temperature and stirred overnight (*ca.* 8 hours). The resulting precipitates were collected *via* vacuum filtration and rinsed with ethanol, yielding **MNIMP** as orange-yellow powder (4.6 g, 55.7% yield). Melting point of

MNIMP: 120.5–125.1 °C (at standard atmospheric pressure). ^{1}H NMR (Fig. S1 and S2, ESI†), ^{13}C NMR (Fig. S3 and S4, ESI†), and HRMS (Fig. S5, ESI†) measurements were performed to confirm the chemical structure of **MNIMP**, with the peak data summarized as follows. ^{1}H-NMR (600 MHz, DMSO-d$_6$) of **MNIMP**, δ (ppm): 12.94 (s, 1H), 8.98 (s, 1H), 7.93 (dd, 1H, J_1 = 8.63, J_2 = 2.39 Hz), 7.87 (d, 1H, J = 2.50 Hz), 7.67 (dd, 1H, J_1 = 7.72, J_2 = 1.80 Hz), 7.56 (d, 1H, J = 8.65 Hz), 7.45 (t, 1H, J_1 = 15.63, J_2 = 7.87 Hz), 7.01–6.94 (m, 2H), 3.96 (s, 3H). ^{13}C NMR (151 MHz, DMSO-d$_6$) of **MNIMP**, δ (ppm): 165.9, 161.1, 152.9, 146.6, 143.9, 134.6, 133.1, 120.6, 119.8, 119.7, 117.3, 117.1, 107.4, 56.9. HRMS of **MNIMP**: m/z 273.0829 [(M + H)$^+$], calcd 273.0797.

Preparation of the MNIMP film

An MNIMP film was drop-cast on a glass slide substrate using a THF solution (10 mM). The film was dried in air before using. Average thickness of the original state: (5.81 ± 0.26) μm; average thickness after self-assembly: (6.99 ± 0.19) μm.

Calculation of LOD

The fluorescent patterns were quantified by two metrics: total intensity and mean gray values. The relationship between these values and the contact pressure is plotted into a line graph and fitted into linear functions. The LOD was calculated using the following equation: LOD = $3S_d/k$. S_d refers to the standard deviation of the color intensities or gray values of the as-prepared film. k is the slope of the fitted linear function.

Working mechanism of the CNN model

In order to make the CNN model more compatible with texture recognition and classification, we made some customized settings and modifications on the ResNet-18 architecture. Detailed description of the principles of CNN with their functional modules and the architecture of ResNet-18 are indicated in the ESI† (Section S3). In the input layer, a series of data preprocessing operations were performed to uniformly crop the image to a size of 224 × 224, which ensures the consistency with the required image size of the first convolutional layer of ResNet-18. To break through the limitation of the sample size collected manually, the richness of the training set was enlarged using a data augmentation strategy. Concurrently, the transfer learning was employed to pre-train the model, thereby enhancing the efficiency and accuracy of image recognition and classification in the training phase. In the training process, we added a back-propagation strategy to continuously optimize the relevant parameters and introduced a patience value to prevent the model from overfitting. For instance, if the accuracy is unchanged or decreased after certain cycles of training, it would stop running in advance. The confusion matrix and evaluation index results were output after short-time running.

Results and discussion

Photophysical behaviours

According to the molecular design, the phenolic hydroxyl and methoxy groups function as electron donors due to their lone pair electrons, while the nitro group acts as an electron acceptor owing to its strong electron-withdrawing nature (Fig. 1A). To verify the asymmetric distribution of frontier molecular orbitals characteristic of donor–acceptor (D–A) pairs, we performed quantum chemical calculations based on density functional theory (DFT) using its lowest-energy conformation (Fig. 1B). As shown in Fig. 1C, the highest occupied molecular orbital (HOMO) of **MNIMP** is primarily localized on the phenol moiety, whereas the lowest unoccupied molecular orbital (LUMO) is predominantly distributed on the nitrobenzene moiety. This partial charge separation, combined with the twisted conformation of **MNIMP**, favors the formation of the anticipated twisted intramolecular charge transfer (TICT) state. The charge difference density (CDD) analysis in Fig. 1D reveals evident charge depletion on the phenol moiety and significant charge accumulation on the nitrobenzene unit. The calculated charge centroids (C$^+$/C$^-$) of **MNIMP** demonstrate a charge transfer distance (D_{CT}) of 4.24 Å (Table S1, ESI†), providing direct evidence for TICT formation. The TICT behavior of **MNIMP** was further corroborated by its polarity-dependent spectral characteristics. As shown in Fig. 1E, the UV-Vis absorption spectrum displays a bathochromic shift (364–379 nm) with increasing solvent polarity, indicative of a positive solvatochromic effect intrinsic to TICT. Similarly, the emission spectrum exhibits a progressive bathochromic shift and progressively increasing Stokes shifts with solvent polarity (Fig. 1F and Table S1, ESI†). The twisted molecular conformation with rotatable single bonds facilitates intramolecular motion, promoting TICT formation in polar solvents while suppressing undesirable π–π interactions in the aggregated state, thereby imparting aggregation-induced emission (AIE) characteristics to the compound. As illustrated in Fig. 1G, **MNIMP** dissolved in pure THF (0% water fraction, f_w) exhibits weak emission at 563 nm. Samples with 0–99% f_w were extracted and examined under a fluorescence microscope under wet-state conditions (Fig. S6, ESI†). When the water fraction (f_w) is between 0% and 80%, the **MNIMP** molecules do not form aggregates and remain dissolved. At this stage, the molecules are highly solvated. As the water content increases, the polarity of the water–THF solvent mixture gradually rises. According to the TICT principle, higher solvent polarity forces the molecule to twist, leading to an intramolecular charge separation. Polar solvents with high dielectric constants effectively stabilize this separated charge state through electrostatic interaction, lowering the energy gap. This stabilization facilitates TICT state while narrowing the energy gap between TICT and ground states, thereby significantly accelerating non-radiative transitions (*e.g.*, thermal dissipation, vibrational relaxation and internal conversion) and diminishing radiative transition probability. Consequently, **MNIMP** exhibits progressively quenched fluorescence across 0–80% water content due to dominant TICT behavior. Notably, at 90% and 99% f_w, **MNIMP** shows substantial emission enhancement (3.5-fold increase compared to 0% f_w) and a fluorescent lifetime of 0.85 ns (Fig. S7 and Table S1, ESI†). The distinct emission difference between 0% and 99% f_w is visually discernible (Fig. 1H). At 90–99% f_w, fluorescence microscopy

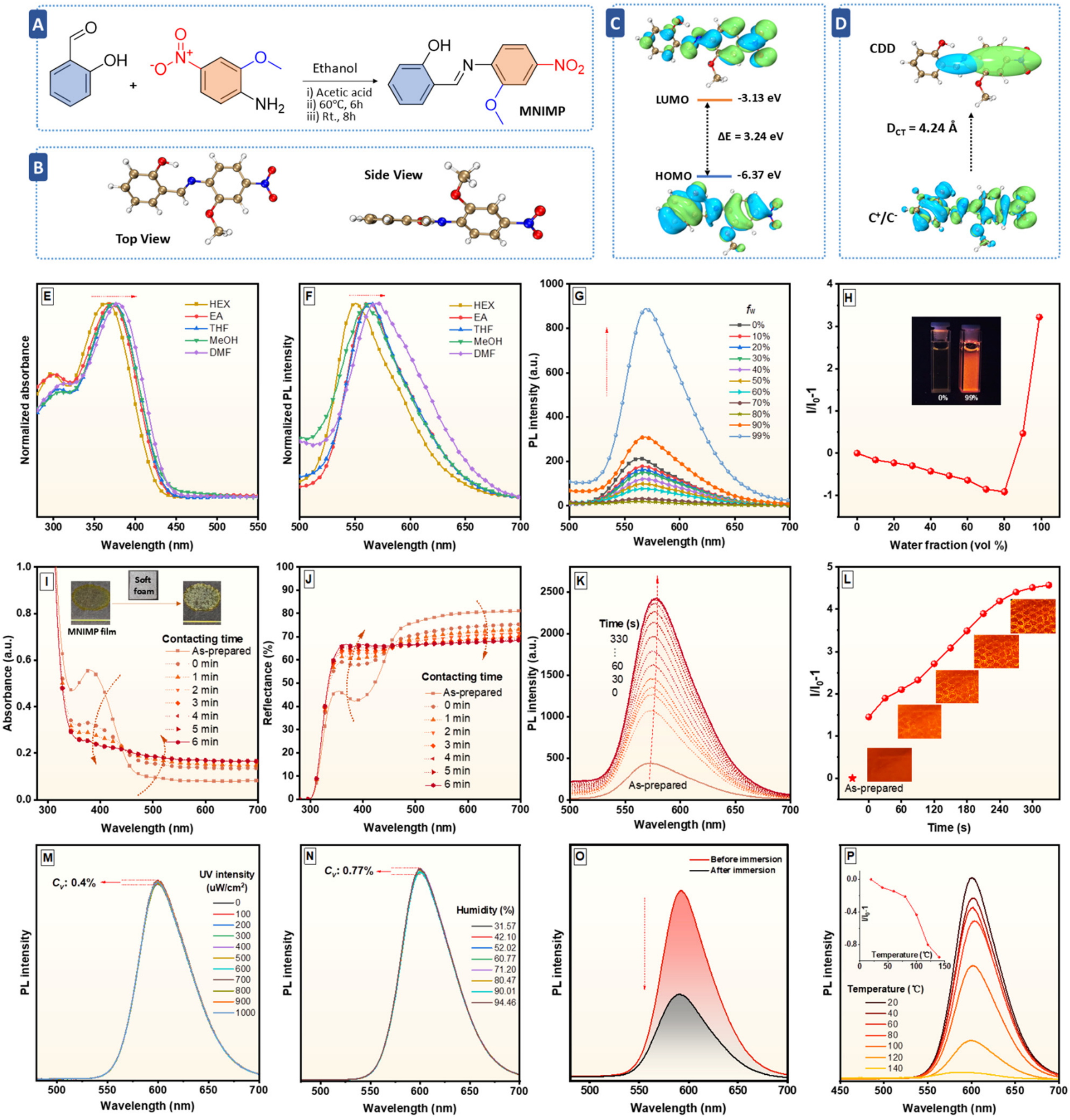

Fig. 1 (A) Synthesis route and molecular structure of **MNIMP**. (B) Top-view and side-view of **MNIMP**'s lowest energy conformation derived from density functional theory (DFT) calculation. (C) HOMO and LUMO orbital distribution of **MNIMP** calculated using B3LYP/6-31+G* basis set. (D) Charge difference densities (CDD) between S_0 and S_1, DCT and C^+/C^- calculated using the PCM(THF)/TD-B3LYP/6-31+G* basis set. The green and blue regions indicate the density increment and decrement, respectively. (E) Normalized absorption and (F) emission spectra of **MNIMP** in organic solvents with increasing polarity. Concentration: 100 μM. (G) Emission spectra of **MNIMP** in THF–water mixtures with different water factions with 414 nm excitation wavelength. Concentration for both absorption and emission measurements: 100 μM. (H) Growth rate of **MNIMP** ($I/I_0 - 1$) in THF–water mixtures as a function of f_w. Inset: Photos of **MNIMP** in solution and aggregation states. (I) Time-dependent change of UV-Vis absorption spectra and (J) reflectance spectra of **MNIMP** film after contact with a piece of soft foam. (K) Change of the emission spectrum of **MNIMP** film over time. Excitation wavelength: 414 nm, concentration: 100 mM. (L) Growth rate ($I/I_0 - 1$) as a function of time. Inset: Photographs of the **MNIMP** film after contact with a piece of soft foam captured at different time. (M) Emission spectra of **MNIMP** under UV exposure with increasing intensity (0–1000 μW cm^{-2}). (N) Emission spectra of **MNIMP** under humidity environments with increasing relative humidity (RH). (O) Emission spectra of **MNIMP** before and after water immersion. (P) Emission spectra of **MNIMP** measured at gradually increased temperature (20–140 °C). Inset: Trend of the maximum emission intensity with temperature. Excitation wavelength for all the emission measurements: 414 nm.

images confirmed **MNIMP** precipitation into micro-scale aggregates with complete molecular desolvation, rendering the TICT mechanism inoperative. The AIE mechanism subsequently dominates, leading to substantial fluorescence enhancement owing to restricted intramolecular motion. The fluorescence quantum yield of **MNIMP** in THF solution is below 1%, while it increases to 4.2% in the solid state, fully confirming the AIE phenomenon. Collectively, the photophysical properties of **MNIMP** demonstrate a synergistic interplay between AIE and TICT mechanisms.

The **MNIMP** film was prepared *via* drop-casting onto a glass slide, exhibiting uniform particle size distribution and high surface flatness. Notably, it generates pronounced spectral responses upon physical contact with textured target objects. The as-prepared **MNIMP** film displays a prominent absorption peak centered at 382 nm (Fig. 1I), analogous to its behavior in high-polarity solvents, confirming the TICT state. When physically contacted with soft foam (a target object with periodic texture), the film develops a corresponding patterned imprint. A tailing peak emerges in the long-wavelength region (450–700 nm) due to light scattering from the imprinted pattern, accompanied by attenuation of the original absorption peak. As revealed by the *in situ* reflectance spectrum (Fig. 1J), the pristine **MNIMP** film shows lower reflectivity in the short-wavelength range, attributable to molecular absorption. Conversely, the long-wavelength reflectivity increases sharply owing to reduced molecular absorptivity in this region. Physical contact with the target object induces surface roughening and grain pattern formation on the film. This structural alteration enhances light scattering while reducing molecular absorption. Consequently, long-wavelength reflectivity decreases while short-wavelength reflectivity increases. Remarkably, the fluorescence signal of the **MNIMP** film shows pronounced responsiveness. The pristine film exhibits weak fluorescence with an emission maximum at 570 nm (Fig. 1K). Upon contact with the target object, the fluorescence intensity immediately intensifies. After removing the object, fluorescence continues to increase progressively, stabilizing after 5 minutes. As shown in the peak value trend (Fig. 1L), the final fluorescence intensity achieves a 4.6-fold enhancement compared to the initial state, demonstrating high signal contrast. Initially, the as-prepared **MNIMP** film exhibits a quantum yield below 1% due to its amorphous state. After five minutes of contact with textured objects, it undergoes complete ordered self-assembly, resulting in a significant increase to 3.3%, demonstrating substantial enhancement in fluorescence efficiency. Concurrently with fluorescence amplification, the film develops increasingly distinct texture patterns (Fig. 1L), readily observable by the naked eye.

To assess the robustness of **MNIMP**, comprehensive environmental stability tests were conducted. Photostability evaluations under UV irradiation (5 min) confirm negligible wavelength or intensity variance, where the variation coefficient (C_v) is calculated to be as low as 0.40% (Fig. 1M). Even under continuous high UV exposure (1000 $\mu W\ cm^{-2}$), **MNIMP** exhibits no detectable photobleaching or spectral shift, which highlights its superior photostability and anti-photobleaching performance (Fig. S8, ESI†). Humidity-controlled experiments (0–90% RH) reveal no wavelength shift in emission spectra, accompanied by highly stable fluorescence intensity (C_v = 0.77%), as indicated in Fig. 1N. In addition, the material demonstrates persistent fluorescence stability under high humidity conditions up to 90% (Fig. S9, ESI†). Notably, this material shows rapid fluorescence quenching (approximately 54% reduction) within 60 s water immersion (Fig. 1O), attributed to partial dissolution of the solid–liquid interface, which is a phenomenon aligning with AIE.[71] Consequently, water immersion should be strictly avoided in practical deployments. Thermal cycling tests demonstrate temperature-dependent emission behavior: fluorescence gradually weakens with heating but retains over 50% initial intensity at 100 °C (Fig. 1P). Material functionality is compromised above 120 °C, indicated by irreversible spectral distortion with severe quenching effect. The thermal stability test confirms that the **MNIMP**'s operational temperature range spans from ambient conditions up to 100 °C.

Thermogravimetric analysis (TGA) results (Fig. S10A, ESI†) demonstrate that the onset decomposition temperature ($T_{d,onset}$) reaches 237.5 °C with merely 5% mass loss before this stage, indicating a relatively high thermal stability. Upon exceeding this point, rapid decomposition commences. The derivative thermogravimetry (DTG) curve derived from TGA differentiation reveals a distinct rate peak at 316.8 °C (minimum in a derivative plot), defined as the maximum decomposition rate temperature ($T_{d,max}$) where the degradation rate accelerates to *ca.* 2% s^{-1}. A residual mass of 1.3% at 600 °C aligns with the anticipated carbonization tendency of typical aromatic small molecules. Complementary differential thermal analysis (DTA) reveals that the sharp endothermic peak at 125.1 °C corresponds to material melting (Fig. S10B, ESI†). The broad endotherm near 316.5 °C aligns with the TGA-derived $T_{d,max}$, verifying backbone thermal degradation. Crucially, under an air atmosphere, two partially overlapping exotherms emerge between 320 and 550 °C (with peak temperatures at 346.2 °C and 509.7 °C, respectively), indicating stepwise oxidation. According to thermal stability hierarchy, the former is assigned to oxidative degradation of methoxy and nitro groups, while the latter stems from deep oxidation of benzene rings. The combined thermal analysis confirms the thermal reliability of this conjugated small-molecule material within the normal operational temperature window (−10 to 40 °C). The lowest phase transition temperature exceeds the upper limit by >80 °C, eliminating the risk of solid-state transition during operation. Moreover, $T_{d,onset}$, $T_{d,max}$ and oxidation exotherms locate in thermally inaccessible zones. Consequently, thermal deformation, decomposition, and oxidative degradation hazards are precluded under application scenarios.

Morphology analysis and mechanism study

To investigate the working mechanism behind the unique fluorescent response of the **MNIMP** film, we conducted morphological characterization using scanning electron microscopy (SEM). As shown in Fig. 2A, the film was fabricated by drop-casting a THF solution of **MNIMP**. SEM images demonstrate uniform adhesion of **MNIMP** to the glass substrate

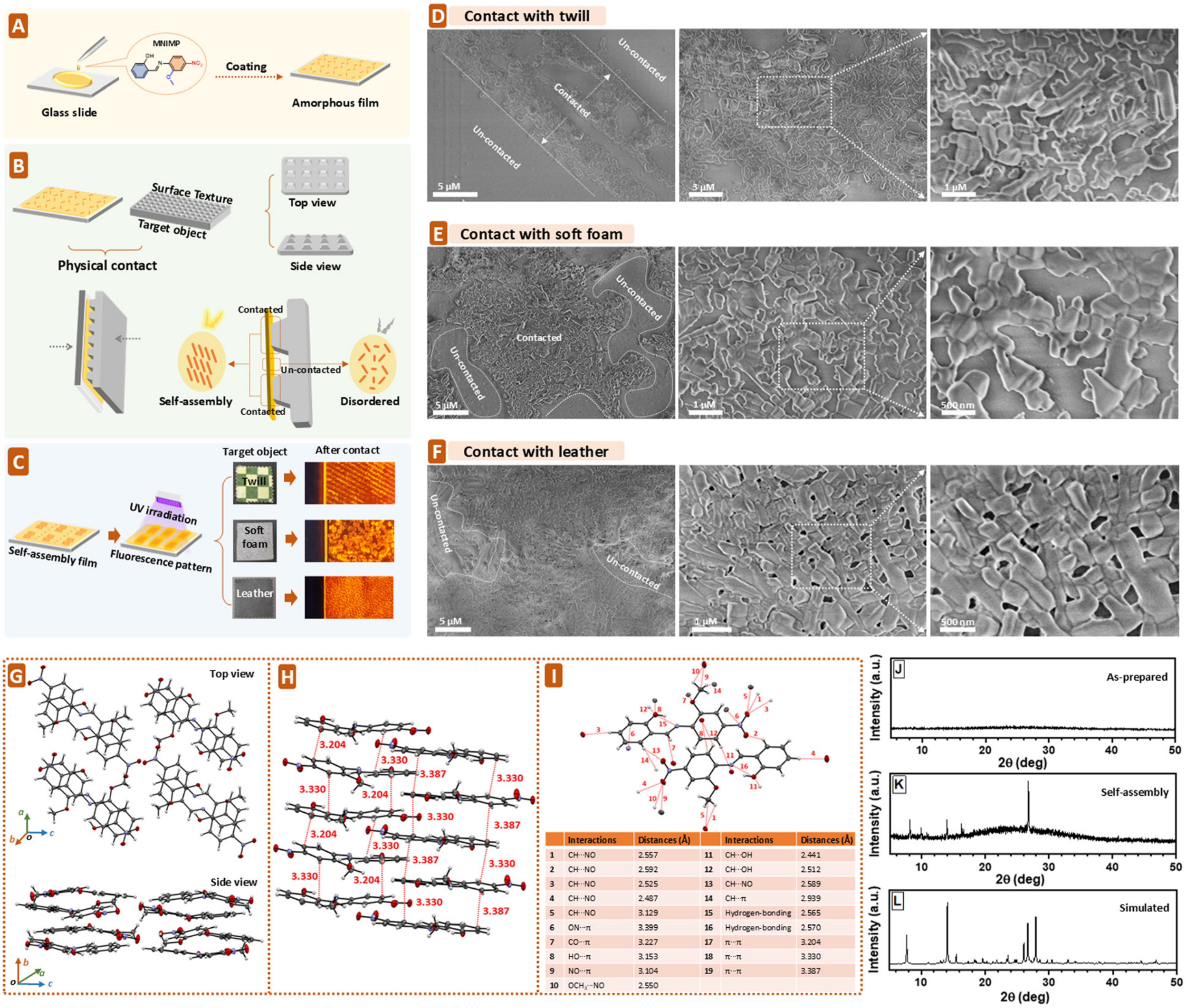

	Interactions	Distances (Å)		Interactions	Distances (Å)
1	CH···NO	2.557	11	CH···OH	2.441
2	CH···NO	2.592	12	CH···OH	2.512
3	CH···NO	2.525	13	CH···NO	2.589
4	CH···NO	2.487	14	CH···π	2.939
5	CH···NO	3.129	15	Hydrogen-bonding	2.565
6	ON···π	3.399	16	Hydrogen-bonding	2.570
7	CO···π	3.227	17	π···π	3.204
8	HO···π	3.153	18	π···π	3.330
9	NO···π	3.104	19	π···π	3.387
10	OCH_3···NO	2.550			

Fig. 2 (A) Schematic illustration showing the preparation of **MNIMP** film using a THF solution (100 mM). (B) Mechanism of the molecular self-assembly of **MNIMP** on the film after contact with a target object. (C) Photographs of fluorescent patterns on the films after physical contact with three textured target objects. Scanning electron microscopy (SEM) images of the film after contact with (D) twill, (E) soft foam and (F) leather. Areas in contacted and not in contact are separated by white dotted lines. (G) Top and side view of a single unit cell. (H) Packing arrangement driven by weak π–π interactions. CCDC 2457590 contains the supplementary crystallographic data.† (I) List of the inter-/intra-molecular interactions in the repetitive unit. PXRD diffractograms of **MNIMP** film (J) before and (K) after contact-induced self-assembly. (L) PXRD diffractograms of **MNIMP** simulated from single crystals.

without well-defined morphological features, suggesting disordered molecular packing (Fig. S11, ESI†). Upon contact with textured target objects, the interaction forces on the film can be classified into two scenarios: contacted and uncontacted regions. Raised surface textures establish physical contact with the film, while recessed textures create gaps, leaving numerous micro-regions uncontacted (Fig. 2B). Under contact pressure, **MNIMP** molecules undergo self-assembly into highly ordered aggregated structures (Fig. 2B). The contact-induced crystallization of amorphous **MNIMP** thin films fundamentally represents a directed phase transition process in which a thermodynamically metastable system overcomes kinetic limitations under external mechanical stimuli. Thermodynamically, although the crystalline phase possesses lower Gibbs free energy, the classical nucleation theory reveals that the high interfacial energy of the pristine amorphous film establishes substantial energy barriers that initially suppress spontaneous phase transition.[72] Mechanical contact reconstructs the system's energy landscape through dual synergistic mechanisms. First, the anisotropic stress field generated at the interface induces directional alignment of molecules, effectively reducing the interfacial energy between nuclei and the amorphous matrix. Second, foreign textured surfaces of target objects act as heterogeneous nucleation templates, providing molecular pre-assembly platforms through physical absorption to significantly decrease the critical nucleation size. Consequently, mechanical stimulation triggers solid–solid phase transition in the **MNIMP** film, where cooperative alignment of nuclei and long-range ordered growth drive the formation of organized structures. This process manifests macroscopically as oriented microdomains exhibiting periodic fluorescent texture resembling the foreign surface textures. According to the aggregation-induced emission (AIE) mechanism, specifically the restriction of intramolecular motion (RIM) theory,[71] the weak fluorescence of the pristine **MNIMP** film originates from its disordered molecular arrangement with substantial intermolecular voids. This structural disorder permits intramolecular motion that suppresses radiative transitions. In contrast, molecular self-assembly reduces free volume and increases steric hindrance, thereby restricting intramolecular motion and enhancing the AIE effect. Conversely, the twisted intramolecular charge transfer (TICT) state thrives in disordered molecular packing due to unrestricted single-bond rotation, which promotes nonradiative decay and weak emission.[57] However, self-assembly partially immobilizes single-bond rotation, hindering TICT state formation. The combined effects of AIE enhancement and TICT suppression explain the fluorescence intensification in contacted regions. As illustrated in Fig. 2C, **MNIMP** films were pressed against three textured targets (twill fabric, soft foam, and leather). Fluorescent patterns emerged shortly after object removal, accurately replicating three surface textures. Since contacted areas correspond to raised textures, the fluorescent patterns faithfully reflect target surface topography, displaying stripe-like, bubble-like, and honeycomb-crack features, respectively (Fig. 2C).

As shown in Fig. 2D, a perthitic structure emerges on the **MNIMP** film after contact with twill fabric. The uncontacted areas retain their amorphous morphology, consistent with the original state. Enlarged images reveal that the perthitic structure comprises a collection of fragmented nanoflakes with well-defined shapes and sharp boundaries. These nanoflakes interconnect to form micron-sized domains in specific regions, ultimately creating an interlaced textured surface. When contacting soft foam, **MNIMP** undergoes surface-position-dependent self-assembly, resulting in macroscopically distinct patterns compared to twill imprinting (Fig. 2E). However, high-magnification imaging confirms that the fundamental structural units remain similar fragmented nano/micro-flakes, as observed in Fig. 2D. Fig. 2F displays the film morphology after leather contact. The leather's fine grain texture enables molecular self-assembly across most film areas through intimate surface contact. At high magnification, these self-assembled structures resemble those formed by previous targets. Owing to complete interfacial contact, **MNIMP** molecules achieve thorough self-organization, producing extensively interwoven nano–micro textures. In summary, regardless of the target type, the **MNIMP** film consistently replicates surface textures through spatially selective molecular self-assembly.

Single crystals of **MNIMP** were grown by vapor diffusion in a THF–ethanol solution. Based on single-crystal analysis, **MNIMP** crystallizes in the monoclinic crystal system with the space group $P2_1/n$, and its asymmetric unit contains two independent **MNIMP** molecules (Fig. 2G and Table S2, ESI†). Within the molecular structure, the dihedral angles between the two benzene ring planes measure 28.12° and 15.26°, respectively, indicating a certain degree of conformation twisting. It not only facilitates the AIE mechanism but also provides a structural basis for modulating the TICT fluorescence. Analysis of the stacking pattern along the *b*-axis reveals that adjacent **MNIMP** molecules adopt an antiparallel arrangement (Fig. 2H). This specific packing mode arises from the synergistic effects of dipole–dipole interactions driven by the intrinsic D–A pairs, combined with π–π interactions. One set of molecules stacks alternately along the longitudinal direction with π–π interaction distances of 3.204 Å and 3.330 Å, while another set exhibits alternating π–π stacking distances of 3.387 Å and 3.330 Å. These π–π interaction distances are relatively large, resulting in limited overlap of π-electron clouds between adjacent molecules. Consequently, the interaction strength is weaker compared to typical fused polycyclic aromatic hydrocarbons. Such attenuated π–π interactions effectively circumvent the fluorescence quenching caused by excimer-induced forbidden transitions commonly observed in strong π-stacking systems. Clearly, both dipole–dipole and π–π interactions guide long-range ordered molecular stacking and serve as the primary driving forces for molecular self-assembly. The crystal lattice contains numerous other weak intermolecular forces, such as CH···NO and CH···π interactions (Fig. 2I). These weak forces effectively rigidify molecular conformations and restrict intramolecular motions (*e.g.*, rotation and vibration) in the excited state, thereby enhancing the AIE behavior in ordered aggregated states, particularly in the crystalline phase. Consequently, upon self-assembly into an ordered crystalline state, **MNIMP** exhibits a significant enhancement in fluorescence intensity. Powder X-ray diffraction (PXRD) was conducted to verify changes in molecular ordering of **MNIMP**. As shown in Fig. 2J, the as-prepared **MNIMP** film exhibits no discernible Bragg diffraction peaks, with scattering intensity remaining near baseline levels, which confirms the absence of ordered structures and indicates an amorphous phase. Upon contact with a textured object, the film develops structural ordering, resulting in distinct diffraction peaks within the small-angle region (*e.g.*, at 8.1°, 9.9°, and 13.9°), signifying the formation of long-range ordered structures (Fig. 2K). Notably, a prominent sharp peak at approximately 26.8° corresponds to an interplanar spacing of 3.33 Å, as calculated by Bragg's law. This spacing aligns precisely with the antiparallel molecular layer distance derived from single-crystal analysis driven by π–π stacking and dipole–dipole interactions (Fig. 2L). The sharp contrast in PXRD patterns conclusively demonstrates the highly ordered self-assembly of **MNIMP** *via* intermolecular interactions after contacting the target object.

Sensitivity and response rate of the tactile sensor

The **MNIMP** film, which undergoes molecular self-assembly accompanied by distinct fluorescence responses under contact force, demonstrates potential as a tactile sensor for object identification through texture recognition. For tactile sensing applications, sensitivity and response rate represent critical performance metrics. As shown in Fig. 3A, we conducted an *in situ* control experiment by mounting a **MNIMP** film on a fluorescence microscope stage prior to soft foam contact. Contact pressure was systematically increased *via* incremental

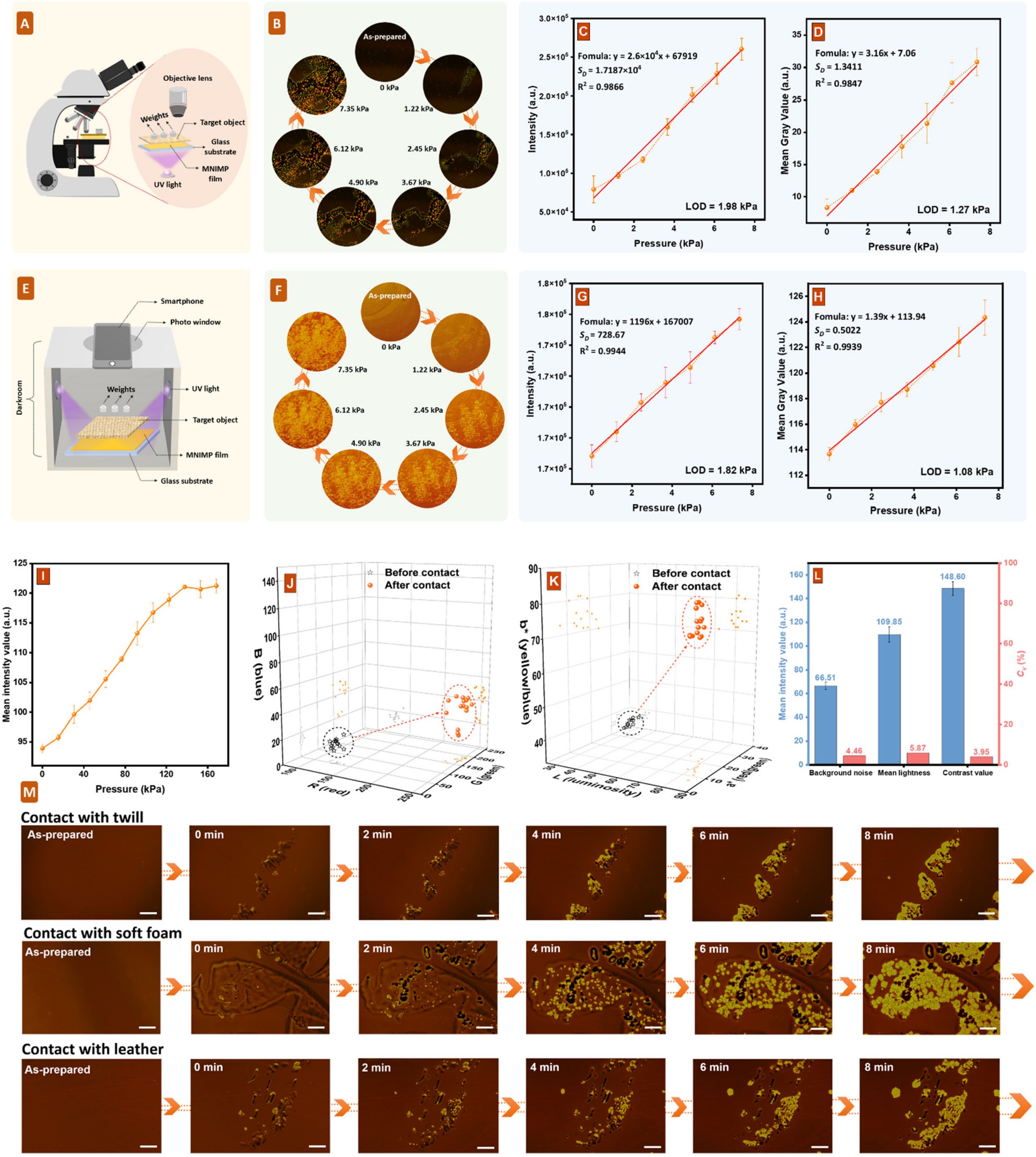

Fig. 3 (A) Schematic illustration of the pressure control experiment and *in situ* photograph of fluorescent patterns under a fluorescence microscope. (B) The change of fluorescent patterns captured using the fluorescence microscope with the increase of contact force. Variations of (C) color intensity and (D) mean gray value as a function of contact force (n = 3). (E) Schematic diagram showing the pressure control experiment in a dark box and the *in situ* photographing of fluorescent patterns. (F) The change of fluorescent patterns with the increase of contact force. Variations of (G) color intensity and (H) mean gray value as a function of contact force (n = 3). (I) Variations of color intensity with increasing contact force showing the response range. (J) RGB and (K) lab values of multiple random points collected from texture imaging. (L) Mean and C_v values of the baseline noise, the imaging signal and the fluorescence contrast. (M) Fluorescence microscope images of **MNIMP** films after contacting with three target objects (*i.e.*, twill, soft foam and leather) captured at different times. Scale bar: 200 μm.

weight addition, with fluorescent images captured at each pressure increment (Fig. 3B). The pristine **MNIMP** film exhibits weak fluorescence as anticipated. At 1.22 kPa contact pressure, faint fluorescent patterns emerge with blurred boundaries.

Pattern clarity progressively improves with increasing pressure, achieving full substrate coverage at 7.35 kPa. For quantitative analysis, fluorescent images were processed using hue-saturation-intensity (HSI) color space to extract pattern lightness values (Fig. 3C). Linear fitting yields the equation $y = 2.6 \times 10^4x + 67\,919$ ($R^2 = 0.9866$), with a calculated limit of detection (LOD) of 1.98 kPa based on standard deviation and slope. This kPa detection threshold indicates high tactile sensitivity. Gray value analysis provides complementary characterization of fluorescence intensity in dark-field images. Compared to HSI analysis, this method prioritizes intensity changes while minimizing wavelength variation interference. As depicted in Fig. 3D, the mean gray value of the pristine film remains low but increases linearly with pressure ($y = 3.16x + 7.06$). The derived LOD (1.27 kPa) aligns closely with the HSI-based detection limit, confirming measurement consistency.

This quantitative analysis was subsequently replicated in a dark-box setup equipped with a stabilized UV source and smartphone camera for imaging capabilities (Fig. 3E). Following the configuration in Fig. 3A, a **MNIMP** film was affixed to the dark box base and subjected to incremental pressure *via* soft foam contact. Fluorescent patterns gradually emerge upon pressure application, becoming clearly visible at 2.45 kPa (Fig. 3F). Color intensities and mean gray values were independently quantified and plotted against contact pressure. As shown in Fig. 3G, color intensity exhibits linear pressure dependence ($R^2 = 0.9944$), yielding 1.82 kPa LOD based on slope and S_d. Notably, the mean gray value analysis (Fig. 3H) demonstrates superior linearity ($R^2 = 0.9939$) and enhanced data precision, achieving an LOD of 1.08 kPa that underscores heightened sensitivity. These LOD values align closely with those from prior methodologies, all falling within the kPa range. Such sensitivity spans typical tactile force magnitudes, suggesting broad applicability across force-sensing scenarios.

To measure the mechanical response range of the **MNIMP** film, we systematically adjusted external pressure gradients while simultaneously monitoring its average fluorescence intensity. As shown in Fig. 3I, the fluorescence intensity demonstrates a strong positive correlation with applied pressure within the 0–140 kPa range. Beyond the critical threshold of 140 kPa, the intensity stabilizes at a plateau, indicating the **MNIMP** film has reached its maximum detection range. This 0–140 kPa operational range aligns well with typical tactile force levels and matches the interactive force range between sensors and target objects. Given the sensitivity profile and detection range, the tactile sensor achieves non-destructive detection of surface textures while maintaining high accuracy across moderate yet sufficiently broad pressure conditions. This combination enables precise acquisition of surface texture information under biologically relevant tactile forces, which is a key advantage for simulating human tactile perception mechanisms. To validate the sensor's signal contrast in texture imaging, we performed comparative analyses in both RGB and lab color spaces. As shown in Fig. 3J, the initial sensor film exhibits low *G*/*B* values but a relatively higher *R* value (though still within low ranges), consistent with its weak orange-red fluorescence at the starting state. Following texture imaging, the output signals show significant enhancement in *R* and *G* values, with the *R* channel approaching saturation, which matches the observed blue-shift and intensity boost in its emission spectra. The lab color space analysis (Fig. 3K) reveals parallel changes: increased L^* (luminosity) and b^* (yellow-blue axis) values alongside decreased a^* (green-red axis) values, indicating both hypsochromic shift and light intensity enhancement. Repeated measurements generate two distinctly separated clusters in both color spaces, demonstrating high discriminative capability that establishes a robust foundation for machine vision analysis.

Signal stability serves as a key indicator of robustness in tactile sensors. For the **MNIMP** tactile sensor with texture imaging and recognition function, this stability is quantified through three parameters, including (i) baseline noise in the initial state, (ii) imaging signal variation after activation, and (iii) fluorescence contrast during texture detection. Through repeated fluorescence imaging experiments, these parameters were systematically evaluated using C_v measurements. As demonstrated in Fig. 3L and Table S3 (ESI†), the baseline noise shows minimal variation with a C_v of 4.46%, indicating excellent signal consistency at rest. The activated imaging signals and fluorescence contrast exhibit similarly low variability (5.87% and 3.95% C_v, respectively), confirming stable performance throughout operation cycles. These results collectively demonstrate the sensor's reliable signal stability in the critical functional phase, which is a fundamental requirement for practical texture recognition applications. The response rate of the **MNIMP** tactile sensor was evaluated through *in situ* fluorescence microscopy observation. The **MNIMP** film initially exhibits weak fluorescence but rapidly develops a faint outline upon contact with twill fabric (Fig. 3M). This outline emits yellow fluorescence within seconds and achieves maximum brightness within 4 minutes, consistent with the spectral response shown in Fig. 1K. Similar fluorescence activation kinetics are observed for soft foam and leather contacts, indicating uniform response rates across different textures (Fig. 3M). As previously discussed, brightened regions correspond to raised surface textures where **MNIMP** molecules self-assemble into ordered aggregation states, enabling enhanced fluorescence emission. Conversely, regions not in contact retain recessed textures without molecular reorganization, maintaining their original fluorescence intensity. In summary, the **MNIMP** film demonstrates dual capabilities of high sensitivity and rapid response, positioning it as a promising high-performance tactile sensor.

Target object recognition

To verify the application range of the tactile sensor, we tested various target objects with diverse surface texture features, including rubber, sponge, elastic polyester, grid fabric, stripe fabric, *etc.* As shown in Fig. 4A, these materials exhibit significant differences in texture size, surface roughness, orientation trends, texture depth, and distribution density. Upon physical contact with the **MNIMP** tactile sensor, their surface textures are faithfully replicated as fluorescence patterns that mirror the objects' structural characteristics (Fig. 4B). By analyzing fluorescent pattern features, such as periodicity, size, spacing, and interval, target objects can be unambiguously identified

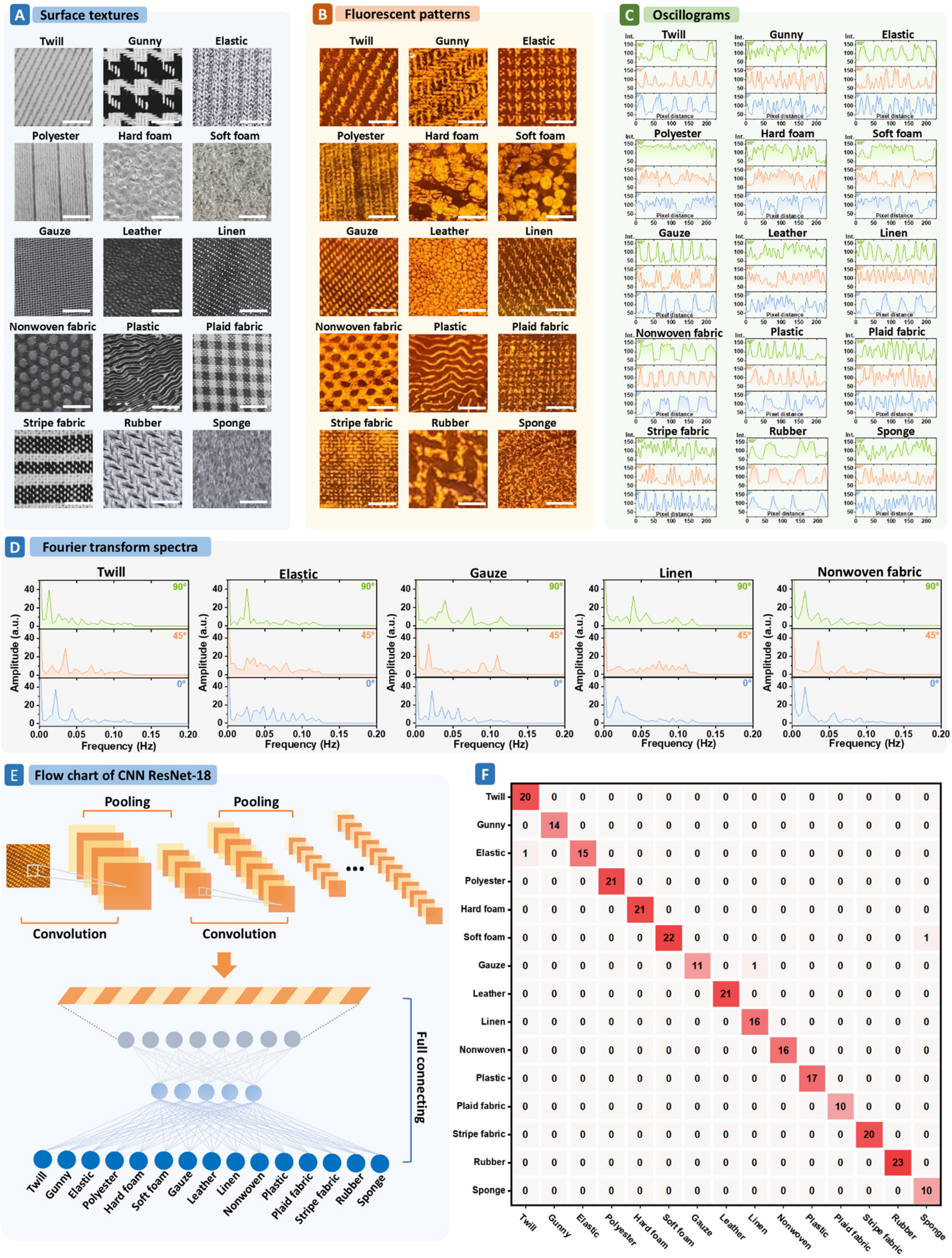

Fig. 4 (A) The real photographs of the surface textures from 15 target objects. (B) Fluorescent images of the corresponding textures imprinted on **MNIMP** films. (C) Intensity oscillograms in the 0°, 45° and 90° directions derived from the textured fluorescence image (horizontal coordinate denotes pixel distance; vertical coordinate denotes color intensity). (D) Fourier transform spectra of representative textured targets (*i.e.*, twill, elastic, gauze, linen and nonwoven fabric) in 0°, 45° and 90° directions. (E) Schematic illustration of the CNN model used for texture recognition and classification. (F) Confusion matrix showing the recognition results of 15 target objects (80% training set and 20% test set).

without direct visual observation or on-site inspection, which is a critical capability for intelligent device applications. This functionality addresses practical challenges where environmental constraints, lighting conditions, or object orientation hinder direct observation. The **MNIMP** tactile sensor records surface textures through tactile perception, enabling remote object characterization when integrated into intelligent devices. This capability significantly enhances remote work efficiency for distant operators. However, real-world scenarios involving numerous targets and recognition tasks would generate large-scale fluorescent images, making manual visual analysis time-consuming and prone to subjective errors.

To overcome this limitation, we developed a computer-aided analysis method. In the HSI color space, bright regions correspond to high color intensity values, while dark regions reflect lower values. By positioning straight lines at specific angles (0°, 45°, and 90°) across fluorescent patterns (Fig. 4C), image processing software extracts pixel-wise color intensities along these profiles, generating oscillograms that correlate with surface textures. The peaks in the oscillograms indicate fluorescence-enhanced raised textures, whereas the valleys correspond to recessed textures with weak emission. These oscillograms exhibit one-to-one correspondence with both fluorescent patterns and target surface textures. As demonstrated in Fig. 4C, periodic oscillograms characterize materials like twill, gunny, elastic, gauze, linen, nonwoven fabric, plaid fabric, and stripe fabric. Despite overlapping periodicities in specific orientations (*e.g.*, gauze and plastic at 0°), multi-angle profiling enables unambiguous identification. Non-periodic materials (polyester, foams, and leather) produce distinct oscillograms through variations in peak/valley trends, densities, and spacings, allowing accurate classification.

Traditional analysis of periodic optical signals often faces limitations from noise interference, waveform overlapping, and subjective misjudgment. To address these challenges, Fourier transform was used to convert the above oscillograms into the frequency domain, enabling effective decoupling of composite optical signals. This approach allows precise localization of dominant periodic components in signals, which enhances the identification of optical signal characteristics. It therefore improves the discrimination efficiency among distinct optical signal types. For fluorescence signals generated by specific textures, pronounced periodic features manifest as sharp single peaks in the Fourier transform spectra. Examples include the primary peaks for elastic (90° direction), linen (0° direction), and nonwoven fabric (45° direction). Subtle periodicities in secondary signals with broader spans, though imperceptible in raw oscillograms, become evident as distinct subsidiary peaks in low frequency region, such as the 0.04 Hz peak for twill (0° direction) and dual peaks at 0.09/0.11 Hz for gauze (45° direction). For complex or weak signals with obscured periodicities, Fourier transform spectra reveal highly distinguishable multi-peak patterns. Representative cases include linen's 10-peak cluster (0.02–0.11 Hz, 45° direction) and elastic's 10-peak cluster (0.01–0.12 Hz, 0° direction), as illustrated in Fig. 4D. Fourier transforms were also performed on ten additional textured objects (Fig. S12, ESI†), demonstrating that single peaks, subsidiary peaks, and multi-peak clusters collectively serve as unique "fingerprint profiles" for precise texture comparison and classification. Thus, the reliability and accuracy are significantly improved. In contrast, non-periodic signals are effectively suppressed after Fourier transform, such as those from blurred imaging areas or incomplete molecular self-assembly. Similarly, strong but non-periodic fluorescent signals (*e.g.*, stray light spots or overexposed regions) are filtered out as noise. These interferences, which hinder conventional oscillogram analysis, are systematically eliminated through Fourier transformation, greatly facilitating texture recognition.

Although oscillographic analysis enables differentiation, the data derived from color space transformations require manual collection and exhibit batch-to-batch variability. Furthermore, occasional image blurring may introduce interference in oscillograms, adversely affecting recognition accuracy. Machine learning, particularly deep learning, excels at processing large-scale datasets with robust error tolerance and background noise immunity, enabling accurate classification. Among machine-learning models, Convolutional Neural Network (CNN) demonstrates exceptional performance in image recognition and classification tasks. The CNN architecture typically comprises input, convolutional, pooling, fully connected, and output layers (Fig. 4E). During operation, convolutional kernels iteratively extract spatial features from input images through matrix operations, with final classification determined by weighted outputs in the fully connected layer. We employed a ResNet-18 network featuring 17 convolution-pooling iterations followed by a terminal fully connected layer (Fig. 4E). This architecture incorporates residual learning to mitigate gradient vanishing/explosion issues while preserving feature integrity across deep layers, enhancing both computational efficiency and classification accuracy. A comprehensive dataset of 1300 fluorescent images was compiled from multiple texture imaging sessions (80–100 images per sample; Fig. S13–S27, ESI†). After 150 training cycles, the test set results are visualized *via* a confusion matrix (Fig. 4F), where columns and rows respectively denote predicted and true classifications. Diagonal elements (darkened cells) indicate correct predictions. The model achieved 98.46% accuracy, with only three misclassifications (one twill, one linen and one sponge). Despite minor errors, statistical analysis confirms reliable classification across all texture types, validating the ResNet-18-based CNN model for multi-class surface texture recognition.

Construction of the texture recognition system

The accurate surface texture imaging capability of the **MNIMP** tactile sensor positions it as a critical functional component for artificial intelligence devices. To establish a comprehensive intelligent system, we implemented hardware integration of the **MNIMP** tactile sensor with embedded machine learning models. As illustrated in the proof-of-concept diagram (Fig. 5A), the system comprises three core components: (i) texture-recording module, (ii) image-processing module, and (iii) data analysis module. The texture-recording module employs a programmable robotic arm integrated with the **MNIMP** tactile sensor. The image-

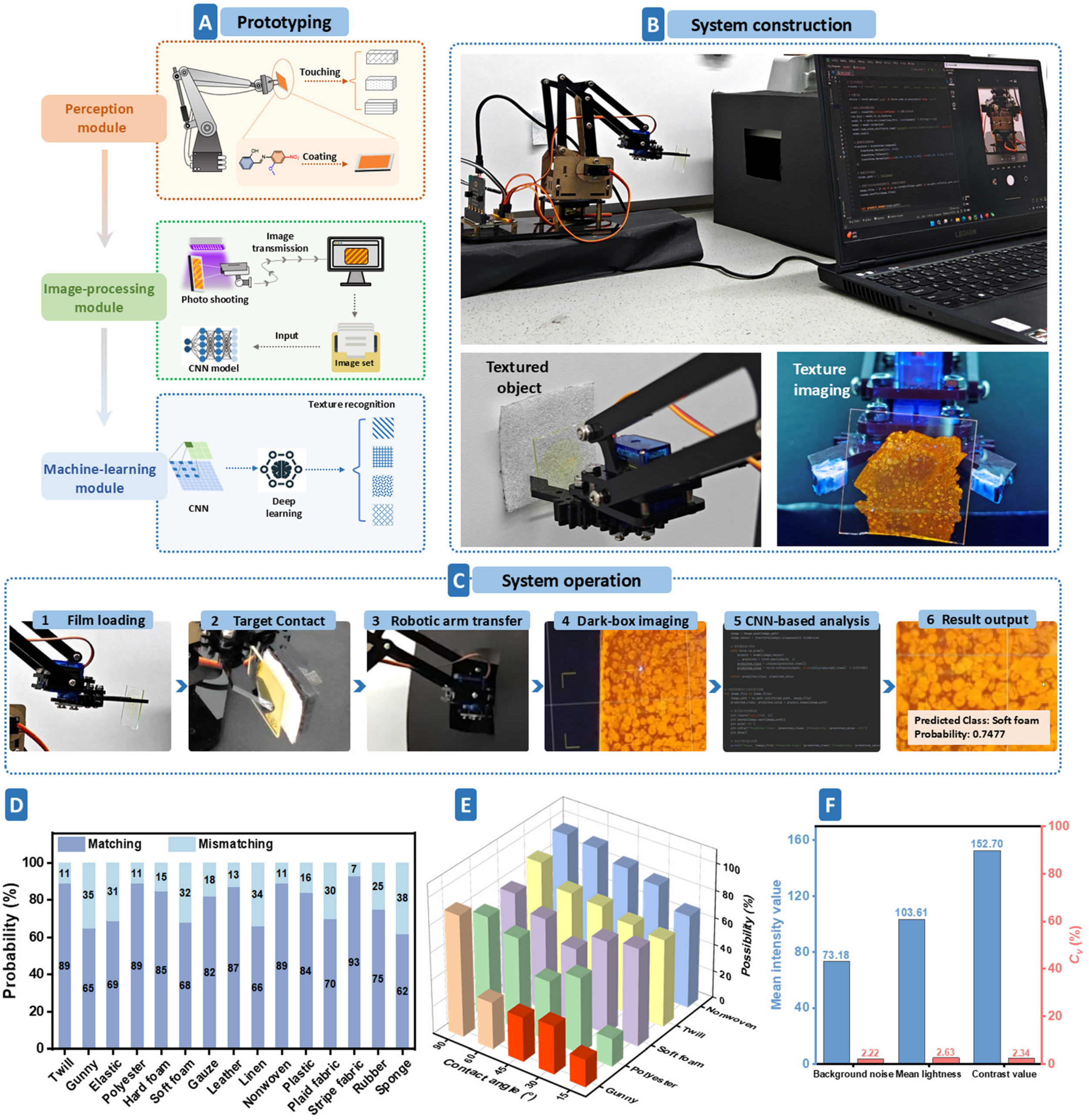

Fig. 5 (A) Conceptual schematic of the intelligent platform developed based on **MNIMP** tactile sensor. (B) Construction of the intelligent platform and (C) the six-step working flow. (D) Inset histogram shows the probability of matching/unmatching of the target objects derived by CNN-based texture recognition. Matching probability refers to the probability of making a correct prediction about the target object. No matching probability refers to the sum of the probability of incorrectly predicting as the other 14 target objects. (E) Probability histograms of matching/unmatching of the target objects derived by CNN-based texture recognition under different contact angles. (F) Mean and C_v values of the baseline noise, the imaging signal and the fluorescence contrast under practical operating conditions.

processing module collects raw imaging data, performs basic operations (*i.e.*, cropping, filtering and optimization), and prepares datasets for machine learning analysis. The data analysis module executes a Python-based CNN algorithm to classify input images and identify target objects. As indicated in Fig. 5B, a functional prototype was constructed following this architecture. The robotic arm positions the **MNIMP** sensor to contact target objects at controlled tactile forces, then transfers the sensor to a dark box for UV-illuminated imaging of fluorescent patterns. Captured images are processed by the CNN model for classification. As illustrated in Fig. 5C, the operational workflow comprises six sequential phases. (i) Film loading: the **MNIMP** tactile film is securely mounted at the robotic arm's distal end, functioning as the active sensing interface. (ii) Target contact: the robotic arm initiates controlled contact between the film and target surface, maintaining 5–10 seconds of sustained pressure exposure before retraction. (iii) Sensor transfer: the robotic arm transfers the sensing module into a dark-box imaging chamber. Under built-in UV illumination (365 nm wavelength, 800–1000 μW cm^{-2}), fluorescent texture patterns become visible on the film. (iv) Dark-box imaging: a portable digital camera integrated within the chamber captures the fluorescent patterns, with raw image data transmitted in real-time to the computer. (v) CNN-based analysis: a pre-trained CNN model automatically initiates texture analysis, executing feature extraction through optimized convolutional layers (The CNN codes are detailed in ESI†). (vi) Result output: The pre-trained model generates prediction outputs within 10 seconds. Finally, the system enters standby mode, enabling manual film replacement for subsequent tasks. A trial operation video using soft foam as a target demonstrates this workflow (as detailed in the ESI†). We conducted perception imaging and recognition experiments on fifteen distinct textured targets using this integrated system. According to the results in Fig. 5D, the system achieved high recognition accuracy across 15 target types. For twill fabric, the CNN model assigned an 89% probability to the correct classification, with $\leq$11% probabilities for other categories. All tested objects received $\geq$60% matching probabilities to their true classes, confirming robust recognition performance.

To validate the contact angle effect, a comparative test was conducted using five soft-textured targets (twill, gunny, polyester, soft foam, and nonwoven). They were fixed to metal rod and pressed against the film at tilt angles of 15°, 30°, 45°, 60°, and 90° for fluorescence imaging. At lower angles, imaging quality declines for some textured targets (Table S4, ESI†), with fluorescence images exhibiting blurring (particularly for gunny). This results from shearing-induced slippage caused by lateral forces under angled contact. The fluorescence images were analysed using CNN model, with classification predictions presented as bar charts (Fig. 5E). Recognition accuracy decreases overall at 15°–45° tilt angles, with significantly lower accuracy for gunny and polyester: gunny shows misclassification, while polyester achieves only 20–50% accuracy. In contrast, nonwoven and soft foam maintain higher accuracy due to their coarse textures. At steeper angles (60° and 90°), misclassification is avoided with substantially improved accuracy. These results confirm reduced recognition accuracy under tilted *versus* vertical contact. Thus, we retain a ‘‘plane-to-plane’’ vertical contact mode, where the **MNIMP** film remains fully parallel to the target surface under normal pressure. It ensures uniform force distribution and eliminates shear interference, thereby optimizing the recognition precision. Stability analysis was conducted under continuous operation, which focused on three key parameters: baseline noise of initial state, signal variation upon activation, and fluorescence contrast in texture imaging. As demonstrated in Fig. 5F and Table S5 (ESI†), the baseline noise exhibits negligible fluctuation (C_v = 2.22%), confirming signal consistency in static conditions. The activated imaging signals and fluorescence contrast similarly show low variability with C_v values of 2.63% and 2.34% respectively, suggesting robust signal stability during operational states.

Conclusions

The novel compound **MNIMP** synergistically integrates aggregation-induced emission (AIE) and twisted intramolecular charge transfer (TICT) mechanisms through a donor–acceptor (D–A) molecular design with conformational twisting. When deposited on glass substrates, **MNIMP** forms uniform drop-casting films with disordered molecular packing, yet undergoes pressure-triggered self-assembly (kPa range) into well-defined nanoflakes upon target object contact. These nanostructures exhibit substantial fluorescence enhancement arising from the cooperative AIE-TICT effect. Since contact areas correspond to raised surface textures, the resulting fluorescent patterns faithfully replicate target morphologies, enabling precise tactile sensing and texture recognition. The **MNIMP** tactile sensor successfully identifies diverse surface features through texture imaging and achieves 98.46% classification accuracy for 15 target types using a CNN model. Notably, this study developed an integrated intelligent system combining **MNIMP** sensors with hardware modules, enabling real-time fluorescence imaging and CNN-based image analysis. This system accomplishes high-accuracy object recognition through physical contact while seamlessly merging tactile sensing with visual feedback, which eliminates complex signal conversion and multimodal data processing. It demonstrates superior performance metrics in sensitivity (kPa level LOD), rapid response (<5 minutes), micron-scale resolution, and cost-effective fabrication. We envision **MNIMP** as a promising high-tech smart material for artificial intelligence applications, particularly in object–machine interaction, robotic manipulation, and machine vision-haptic integration systems. This work establishes a paradigm for developing multifunctional materials that bridge molecular engineering with intelligent device innovation.

Conflicts of interest

There are no conflicts to declare.

Data availability

All relevant data are within the manuscript and the ESI.†

Acknowledgements

This work was financially supported by National Natural Science Foundation of China (Grant No. 51703135).

Notes and references

1 P. H. Thakur, A. J. Bastian and S. S. Hsiao, *J. Neurosci.*, 2008, **28**, 1271–1281.

2 R. Blake, K. V. Sobel and T. W. James, *Psychol. Neurosci.*, 2004, **15**, 397–402.

3 W. Tang, R. Liu, Y. B. Shi, C. Hu, S. J. Bai and H. Zhu, *J. Adv. Res.*, 2020, **21**, 129–139.

4 J. N. Wood and S. M. Waters Wood, *Animals*, 2024, **14**, 284.

5 G. A. Gescheider and J. H. Wright, *Somatosens. Res.*, 2021, **38**, 202–213.

6 J. Tanner, G. Orthlieb, D. Shumate and S. H. Tillery, *Front. Neurosci.*, 2021, **15**, 586740.

7 E. Eklund, E. Svensson and C. Häger-Ross, *Disabil. Rehabil.*, 2009, **31**, 1955–1962.

8 R. J. Heerkens, A. J. Köke, F. J. Lötters and R. J. Smeets, *Pain Manage.*, 2018, **8**, 277–286.

9 R. H. Sun, C. D. Wu, X. Zhao, B. Zhao and Y. Jiang, *Sensors*, 2024, **24**, 195.

10 W. T. Weng, H. P. Huang, Y. L. Zhao and C. Y. Lin, *Sensors*, 2022, **22**, 9545.

11 Y. Xun, J. X. Zhang, W. Li and W. G. Cai, *Prog. Nat. Sci.*, 2007, **17**, 217–221.

12 M. Y. Zhang, X. L. Liu, D. Xu, Z. Q. Cao and J. Z. Yu, *IEEE Trans. Ind. Electron.*, 2019, **66**, 9360–9371.

13 J. S. Zhao, Y. J. Chen, Z. Z. Zhou, J. Y. Zhao, S. Z. Wang and X. Q. Chen, *IEEE Trans. Instrum. Meas.*, 2023, **72**, 2513112.

14 T. Corradi, P. Hall and P. Iravani, *Rob. Biomimetics*, 2017, **4**, 2.

15 S. Gao, Y. N. Dai and A. Nathan, *Adv. Intell. Syst.*, 2022, **4**, 2100074.

16 M. Runowski, P. Woźny, K. Soler-Carracedo, A. Lazarowska, M. Kamiński, N. Majewska, A. Muñoz, J. Moszczyński, S. Sobczak, K. Dave, W.-T. Huang, R.-S. Liu and S. Mahlik, *Mater. Horiz.*, 2024, **11**, 4911–4924.

17 J. Yang, S. Luo, X. Zhou, J. L. Li, J. T. Fu, W. D. Yang and D. P. Wei, *ACS Appl. Mater. Interfaces*, 2019, **11**, 14997–15006.

18 S. Sharma, G. B. Pradhan, A. Chhetry, K. Shrestha, T. Bhatta, S. P. Zhang, D. K. Kim, S. H. Jeong, Y. D. Shin, M. A. Zahed, X. Hui and J. Y. Park, *Nano Today*, 2023, **48**, 101698.

19 Z. B. Xu, J. H. Yan, M. L. Ji, Y. X. Zhou, D. D. Wang, Y. Z. Wang, Z. H. Mai, X. F. Zhao, T. X. Nan, G. Z. Xing and S. S. Zhang, *Micromachines*, 2022, **13**, 2250.

20 C. X. Lu, Y. Gao, X. A. Chan, W. Yu, H. F. Wang, L. Hu and L. W. Li, *Mater. Horiz.*, 2024, **11**, 510–518.

21 G. R. Zhao, X. D. Zhang, X. Cui, S. Wang, Z. R. Liu, L. Deng, A. H. Qi, X. R. Qiao, L. J. Li, C. F. Pan, Y. Zhang and L. L. Li, *ACS Appl. Mater. Interfaces*, 2018, **10**, 15855–15863.

22 C. Dagdeviren, Y. W. Su, P. Joe, R. Yona, Y. H. Liu, Y. S. Kim, Y. A. Huang, A. R. Damadoran, J. Xia, L. W. Martin, Y. G. Huang and J. A. Rogers, *Nat. Commun.*, 2014, **5**, 4496.

23 W. Y. Li, J. H. Hu, Z. Z. Su and D. Wang, *Measurement*, 2022, **187**, 110159.

24 R. Wu, L. Ma, S. Liu, A. B. Patil, C. Hou, Y. Zhang, W. Zhang, R. Yu, W. Yu, W. Guo and X. Liu, *Mater. Today Phys.*, 2020, **15**, 100243.

25 Y. X. Liu, H. Z. Li and M. Zhang, *ACS Appl. Electron. Mater.*, 2021, **3**, 1681–1690.

26 Y. T. Gong, Y.-Z. Zhang, S. Q. Fang, C. Liu, J. Niu, G. J. Li, F. Li, X. C. Li, T. Cheng and W.-Y. Lai, *Appl. Phys. Rev.*, 2022, **9**, 021403.

27 Y. H. Li, S. F. Guo, Z. Q. Su, K. Q. Ding and X. J. Loh, *FlexMat*, 2025, **2**, 4.

28 S. Yang, Y.-J. Cao, K. Han, J.-T. Guo, P.-L. Zheng, L.-Y. Wang, T. Cheng, Y.-Z. Zhang and W.-Y. Lai, *Nano Energy*, 2025, **139**, 110942.

29 T. H. Wang, T. Jin, W. Y. Lin, Y. Q. Lin, H. F. Liu, T. Yue, Y. Z. Tian, L. Li, Q. Zhang and C. L. Lee, *ACS Nano*, 2024, **18**, 9980–9996.

30 X. C. Qu, Z. Liu, P. C. Tan, C. Wang, Y. Liu, H. Q. Feng, D. Luo, Z. Li and Z. L. Wang, *Sci. Adv.*, 2022, **8**, eabq2521.

31 Z. W. Song, J. H. Yin, Z. H. Wang, C. Y. Lu, Z. Yang, Z. H. Zhao, Z. N. Lin, J. Y. Wang, C. S. Wu, J. Cheng, Y. Dai, Y. L. Zi, S. L. Huang, X. L. Chen, J. Song, G. Li and W. B. Ding, *Nano Energy*, 2022, **93**, 106798.

32 P. C. Xing, S. S. An, Y. H. Wu, G. Li, S. Z. Liu, J. Wang, Y. L. Cheng, Y. S. Zhang and X. J. Pu, *Nano Energy*, 2023, **116**, 108758.

33 L. T. Shan, H. A. Zeng, Y. Q. Liu, X. H. Zhang, E. L. Li, R. J. Yu, Y. Y. Hu, T. L. Guo and H. P. Chen, *Nano Lett.*, 2022, **22**, 7275–7283.

34 C. G. Lyu, Y. P. Xiao, Y. Deng, X. Y. Chang, B. Yang, J. C. Tian and J. Jin, *Measurement*, 2023, **216**, 112906.

35 J. W. Yu, Q. W. Niu, H. Wu, X. F. Wang and W. Li, *ACS Appl. Mater. Interfaces*, 2025, **17**, 6604–6613.

36 D. J. Lu, T. Liu, X. J. Meng, B. Luo, J. X. Yuan, Y. H. Liu, S. Zhang, C. C. Cai, C. Gao, J. L. Wang, S. F. Wang and S. X. Nie, *Adv. Mater.*, 2023, **35**, 2209117.

37 L. H. Wang, J. X. Liu, X. J. Qi, X. J. Zhang, H. Wang, M. W. Tian and L. J. Qu, *J. Mater. Chem. A*, 2024, **12**, 8065–8099.

38 X. R. Zhi, S. F. Ma, Y. F. Xia, B. Yang, S. Y. Zhang, K. T. Liu, M. Y. Li, S. H. Li, P. Y. Wan and X. Wang, *Nano Energy*, 2024, **125**, 109532.

39 M. Petz, R. Tutsch, R. Christoph, M. Andraes and B. Hopp, *Measurement*, 2012, **45**, 2288–2298.

40 M. Y. Zhang, Y. Zhang, Y. P. Li, J. H. Wei, L. F. Xu, J. Yuan, Z. Z. Xu, Y. A. Duan and T. Y. Han, *Dyes Pigm.*, 2023, **220**, 111704.

41 R. J. Huang, Y. Xu, J. H. Du, Q. Guan, X. Q. Cai, F. Li, J. D. Wang and W. W. Chen, *Nanoscale*, 2023, **15**, 1806–1812.

42 K. Szendrei, A. Jiménez-Solano, G. Lozano and B. V. Lotsch, *Adv. Opt. Mater.*, 2017, **5**, 1700663.

43 X. X. Zhang, Y. Liu, W. Wei, L. Gao, Y. A. Duan, H. L. Han and T. Y. Han, *Dyes Pigm.*, 2022, **197**, 109916.

44 M. Y. Zhang, L. Zhao, R. X. Zhao, Z. F. Li, Y. Liu, Y. A. Duan and T. Y. Han, *Spectrochim. Acta, Part A*, 2019, **220**, 117125.

45 R. X. Zhao, L. Zhao, M. Y. Zhang, Z. F. Li, Y. Liu, T. Y. Han, Y. A. Duan and K. Gao, *Dyes Pigm.*, 2019, **167**, 181–188.

46 G. Giordano, M. Gagliardi, Y. Huan, M. Carlotti, A. Mariani, A. Menciassi, E. Sinibaldi and B. Mazzolai, *Adv. Sci.*, 2021, **8**, 2100418.

47 Y. Q. Sun, Z. Q. Lei and H. C. Ma, *J. Mater. Chem. C*, 2022, **10**, 14834–14867.

48 V. Gokul, D. Devadiga and T. N. Ahipa, *Dyes Pigm.*, 2021, **195**, 109692.

49 Q. K. Qi, J. Y. Qian, X. Tan, J. B. Zhang, L. J. Wang, B. Xu, B. Zou and W. J. Tian, *Adv. Funct. Mater.*, 2015, **25**, 4005–4010.

50 Y. J. Dong, B. Xu, J. B. Zhang, X. Tan, L. J. Wang, J. L. Chen, H. G. Lv, S. P. Wen, B. Li, L. Ye, B. Zou and W. J. Tian, *Angew. Chem.*, 2012, **124**, 10940–10943.

51 K. Ogumi, K. Nagata, Y. Takimoto, K. Mishiba and Y. Matsuo, *J. Mater. Chem. C*, 2022, **10**, 11181–11186.

52 Z. W. Man, Z. Lv, Z. Z. Xu, Q. Liao, J. X. Liu, Y. L. Liu, L. Y. Fu, M. H. Liu, S. M. Bai and H. B. Fu, *Adv. Funct. Mater.*, 2020, **30**, 2000105.

53 S. Z. Mo, Q. T. Meng, S. L. Wan, Z. Q. Su, H. Yan, B. Z. Tang and M. Z. Yin, *Adv. Funct. Mater.*, 2017, **27**, 1701210.

54 H. Liu, Y. L. Li, L. Wei, Z. J. Ye, J. Yuan and L. H. Xiao, *Nano Today*, 2024, **58**, 102434.

55 R. H. Xu, Q. F. Shen, P. J. Zhang, Z. Wang, Y. Z. Xu, L. J. Meng and D. F. Dang, *Adv. Mater.*, 2024, **36**, 2402434.

56 Y. H. Cheng, J. G. Wang, Z. J. Qiu, X. Y. Zheng, N. L. C. Leung, J. W. Y. Lam and B. Z. Tang, *Adv. Mater.*, 2017, **29**, 1703900.

57 C. Wang, W. J. Chi, Q. L. Qiao, D. Tan, Z. C. Xu and X. G. Liu, *Chem. Soc. Rev.*, 2021, **50**, 12656–12678.

58 Y. Zhang, X. Y. Zhao, L. F. Xu, Y. A. Duan, J. Yuan, Z. F. Li and T. Y. Han, *Sens. Actuators, B*, 2024, **399**, 134834.

59 X. Y. Zhao, Z. H. Liu, Y. A. Duan, Z. Z. Xu, X. Feng, Z. F. Li and T. Y. Han, *Chem. Eng. J.*, 2024, **498**, 155525.

60 A. F. N. Elsyed, G. L. Wong, M. Ameen, M. W. Wu and C. C. Chang, *Int. J. Mol. Sci.*, 2023, **24**, 9941.

61 D. Yang, Y. Y. Ren, J. W. Li, Q. Wang, X. B. Li and X. Z. Qu, *Chem. Eng. J.*, 2022, **431**, 133449.

62 P. J. Shi, Y. A. Duan, W. Wei, Z. Z. Xu, Z. F. Li and T. Y. Han, *J. Mater. Chem. C*, 2018, **6**, 2476–2482.

63 Y. Pei, J. X. Xie, D. X. Cui, S. N. Liu, G. F. Li, D. X. Zhu and Z. M. Su, *Dalton Trans.*, 2020, **49**, 13066–13071.

64 X. X. Ma, L. L. Hu, X. Han and J. Yin, *Chin. Chem. Lett.*, 2018, **29**, 1489–1492.

65 Y. Hou, Y. Li, M. Y. Zhang, X. X. Zhang, Z. Z. Xu, Y. P. Li, Y. A. Duan and T. Y. Han, *Dyes Pigm.*, 2020, **180**, 108505.

66 X. X. Zhang, J. T. Hu, H. L. Han, Z. F. Li and T. Y. Han, *Dyes Pigm.*, 2021, **193**, 109566.

67 L. P. Wang, L. J. Liu, B. Xu and W. J. Tian, *Chem. Res. Chin. Univ.*, 2021, **37**, 100–109.

68 W. D. Yin, Z. M. Yang, S. X. Zhang, Y. Yang, L. X. Zhao, Z. Li, B. Zhang, S. J. Zhang, B. Y. Han and H. C. Ma, *Mater. Chem. Front.*, 2021, **5**, 2849–2859.

69 J. M. Moran, J. H. Hemann and A. S. Greenwald, *J. Orthop. Res.*, 1985, **3**, 49–55.

70 W. T. Yang, M. Y. Xie, X. S. Zhang, X. Y. Sun, C. Zhou, Y. Chang, H. N. Zhang and X. X. Duan, *ACS Appl. Mater. Interfaces*, 2021, **13**, 55756–55765.

71 J. Mei, N. L. C. Leung, R. T. K. Kwok, J. W. Y. Lam and B. Z. Tang, *Chem. Rev.*, 2015, **115**, 11718–11940.

72 J. W. P. Schmelzer, G. S. Boltachev and V. G. Baidakov, *J. Chem. Phys.*, 2006, **124**, 194503.